INSTITUT DE FRANCE
Académie des sciences

Comptes Rendus

Géoscience

Sciences de la Planète

Massimo Scodina, Gabriele Cruciani and Marcello Franceschelli

Metamorphic evolution and *P–T* path of the Posada Valley amphibolites: new insights on the Variscan high pressure metamorphism in NE Sardinia, Italy

Volume 353, issue 1 (2021), p. 227-246

Published online: 29 July 2021

https://doi.org/10.5802/crgeos.65

Les Comptes Rendus. Géoscience — Sciences de la Planète *sont membres du Centre Mersenne pour l'édition scientifique ouverte*
www.centre-mersenne.org
e-ISSN : 1778-7025

Comptes Rendus
Géoscience — Sciences de la Planète
2021, 353, nº 1, p. 227-246
https://doi.org/10.5802/crgeos.65

Original Article — Petrology, Geochemistry

Metamorphic evolution and *P*–*T* path of the Posada Valley amphibolites: new insights on the Variscan high pressure metamorphism in NE Sardinia, Italy

Massimo Scodina [a], Gabriele Cruciani [a] * and Marcello Franceschelli [a]

[a] Dipartimento di Scienze Chimiche e Geologiche, Università di Cagliari – S.S. 554 Cittadella Universitaria, 09042 Monserrato (CA), Italy

E-mails: mskodo85@tiscali.it (M. Scodina), gcrucian@unica.it (G. Cruciani), francmar@unica.it (M. Franceschelli)

Abstract. The Posada Valley amphibolites in the inner zone of Variscan Sardinia are characterized by garnet porphyroblasts containing epidote, titanite, quartz, clinopyroxene, amphibole, and plagioclase concentrated in the garnet core. The matrix is made up of amphibole and plagioclase and fine-grained clinopyroxene and plagioclase. The amphibolites recorded an HP stage, a metamorphic re-equilibration, and a third stage under the greenschist facies. *P*–*T* conditions of stage I (530–650 °C/0.9–1.3 GPa for garnet core and 570–690 °C/1.0–1.4 GPa for garnet rim) were obtained by *P*–*T* pseudosection modelling. The *P*–*T* conditions for stage 2 (T = 600–700 °C/P = 0.5–0.8 GPa) were obtained by applying the same approach to the most retrogressed samples. The Posada Valley amphibolites underwent a cooler evolution, with a thermal peak lower than that recorded by the northward eclogites from the high-grade metamorphic complex of Sardinia.

The proposed geodynamic scenario starts with the subduction of oceanic crust under the peri-Gondwanan terrane in Upper Devonian. The Posada Valley amphibolites were subducted up to maximum depths of 50 km. Subsequently, they reached the subduction channel or were detached from the slab before the eclogite facies conditions were reached.

Keywords. Amphibolite, Metamorphic evolution, *P*–*T* pseudosections, *P*–*T* path, Variscan Sardinia.

Manuscript received 29th March 2021, revised 7th June 2021, accepted 8th June 2021.

1. Introduction

Retrogressed eclogites are widespread in the internal zone of the Variscan chain of Sardinia within the low- to medium-grade metamorphic complex (L-MGMC) and in the high-grade metamorphic complex (HGMC) [also known as migmatite complex; Carmignani et al., 2001].

In the high-grade metamorphic complex hectometre-size lenses of eclogites crop out at Golfo Aranci, Punta Tittinosu, and Punta de li Tulchi (Figure 1(a)). Eclogites of the HGMC are characterized by the occurrence of omphacite relics. The eclogite bodies from the L-MGMC occur as decametric-long lenses inside gneisses and mylonites of the Asinara Island, Giuncana, and the Posada Valley (Figure 1(a)). However, only the metabasite rocks from Giuncana [Cortesogno et al., 2004, Cruciani et al., 2015a] preserve true relics of eclogite facies assemblages (i.e.,

* Corresponding author.

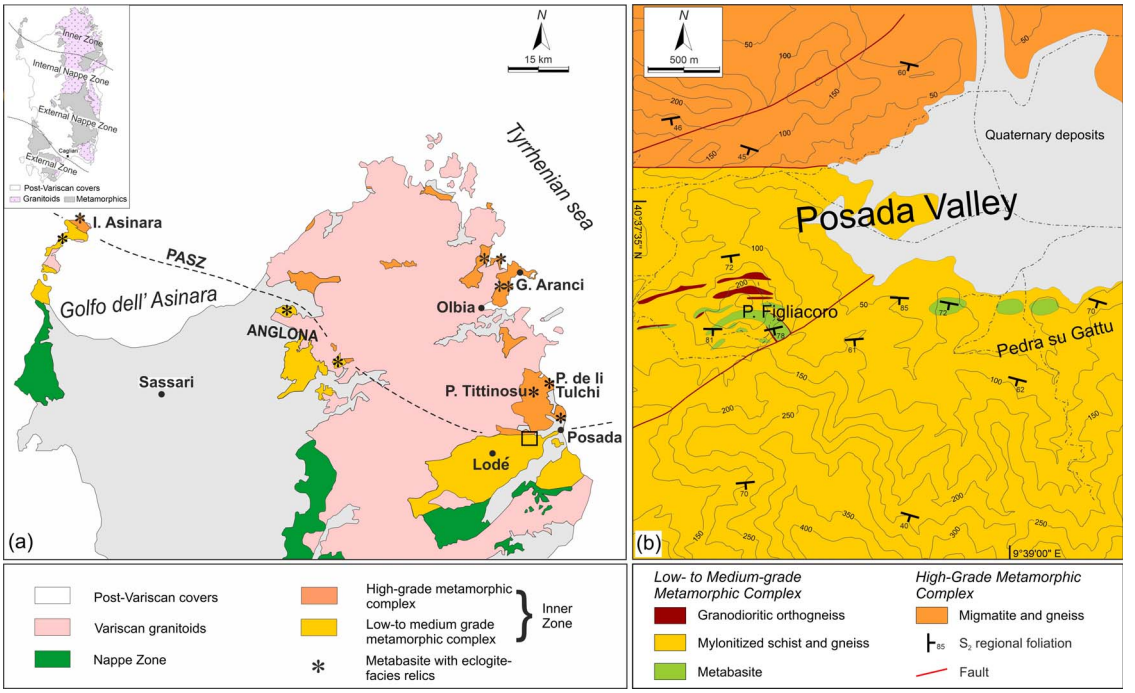

Figure 1. Geological sketch map of (a) northern Sardinia Variscan chain (simplified tectonic sketch map of the Variscan Sardinian chain in the inset), (b) the studied area between P. Figliacoro and Pedra su Gattu localities, in the Posada Valley. PASZ: Posada–Asinara shear zone.

omphacite). Although the shape of the *P*–*T* path is similar between the L-MGMC and HGMC eclogites, a significant difference in temperature (and pressure) has been observed [Cruciani et al., 2012]. The other metabasites from the L-MGMC are still considered eclogites, as well, due to their position along the Posada–Asinara shear zone (Figure 1(a)). The protoliths of Sardinian eclogites are mostly mid-ocean ridge basalt (MORB)-type tholeiites [Cappelli et al., 1992], with the exception of the metabasite from Punta Orvili that exhibits an alkaline affinity [Cruciani et al., 2010], considered by many authors as part of the oceanic crust subducting under the peri-Gondwanan terranes (previously accreted to Laurussia) during the Variscan orogeny.

Thus, the northern part of the medium-grade metamorphic complex is featured by the occurrence of metabasite lenses commonly defined as retrograde eclogites but never studied in depth from a petrographic and metamorphic (*P*–*T* evolution) point of view. In this paper we present a detailed petrological investigation of the Posada Valley amphibolites in order to reconstruct their metamorphic history and *P*–*T* path through *P*–*T* pseudosection modelling. The results will be compared with metamorphic rocks of the inner zone of the Sardinian basement and finally discussed in the geodynamic scenario of the late-Palaeozoic Variscan continent–continent collision.

2. Geological setting

The Sardinian Variscan basement consists of metaigneous to metasedimentary sequences ranging in age from the Cambrian to the lower Carboniferous [Carmignani et al., 2001]. This basement was only slightly affected by the subsequent Alpine Orogeny, and therefore preserves Variscan deformation and metamorphism.

The Sardinian chain has been subdivided into a southern external zone, a central Nappe zone, and an inner (or axial) zone in the northernmost part of the island, which extends to southern Corsica [Faure et al., 2014, Massonne et al., 2018, Cruciani et al., 2021]. For the geological, palaeogeographic reconstruction and the correlation of the Variscan Corsica–Sardinia block with the Maures–Tanneron Massif, the

reader is referred to Rossi et al. [2009], Faure et al. [2014], Schneider et al. [2014], and Gerbault et al. [2018]. In the external and Nappe zones, the basement rocks consist of metasedimentary sequences with middle to late Ordovician volcanics [Cruciani et al., 2013a, 2016]. The arrangement of rock units from the Nappe zone derived from a southward thrusting with km-scale isoclinal folding and syntectonic metamorphism [Carmignani et al., 1994]. The northern part of the inner zone (HGMC) mainly consists of polydeformed sedimentary-derived gneisses and migmatites [Massonne et al., 2013, Cruciani et al., 2014, Fancello et al., 2018], which reached an high metamorphic grade up to the sillimanite + K-feldspar zone [Franceschelli et al., 2005]. Within the HGMC, subordinate rocks like orthogneisses, calc-silicate nodules and metabasite lenses (basic and ultrabasic rocks with eclogite- and granulite facies relics, Franceschelli et al., 2005, 2007, Cruciani et al., 2011, 2015a,b, Scodina et al., 2019, 2020) also occur. The southern L-MGMC is made up of micaschists and paragneisses locally with relics of HP assemblages [Cruciani et al., 2013b] and with sporadic quartzite and metabasite bodies [Cappelli et al., 1992, Cruciani et al., 2010, 2015a]. The metasedimentary rocks reached greenschist- to amphibolite facies conditions and are characterized by an increasing metamorphic grade from south to north [Franceschelli et al., 1982, 1989, Cruciani et al., 2015b]. Near the contact between the HGMC and L-MGMC, there is a sharp increase in metamorphic grade, and the Barrovian isograds are very tight [Carosi et al., 2005].

The boundary between HGMC and L-MGMC, well exposed in the Posada Valley, southern Gallura, and Asinara island, is marked by a dextral transpressional shear zone known as the Posada–Asinara shear zone (PASZ), (Figure 1(a)). U–(Th)–Pb analyses on monazite from the PASZ indicate that the shear zone has been active at ~325–300 Ma in a transpressive setting, in agreement with the ages of the other dextral transpressive shear zones in the southern Variscan belt [Carosi et al., 2020]. Similar ages (~323 Ma) obtained by monazite petrochronology, mark the onset of transpression of the Cavalaire fault in the neighbouring Maures–Tanneron Massif [Simonetti et al., 2020]. The PASZ has been correlated to the Grimaud fault in the Maures–Tanneron massif [Edel et al., 2018 and references therein].

The inner zone of northern Sardinia underwent a polyphase ductile deformation [Carosi et al., 2005, Elter et al., 2010]. The oldest deformation phase (D1), dated at ~345–340 Ma by Di Vincenzo et al. [2004], is well preserved in some areas of the L-MGMC and is related to the collisional and thickening stage [Carmignani et al., 1994], which resulted in HP metamorphism, with metapelites reaching pressures of 1.7 GPa [Cruciani et al., 2013b]. Di Vincenzo et al. [2004] also found apparent ^{40}Ar–^{39}Ar ages of 320–315 Ma for most syn-D2 white mica from the garnet zone of the MGMC. In the HGMC, the D1 deformation is sporadically documented by the transposition of centimetre-sized leucosomes in the migmatites. The D2 deformation phase, which progressively transpose the S1 foliation towards the HGMC, is related to the development of NE verging folds and orogen-parallel dextral shear zones in the field [Carosi and Palmeri, 2002]. The resulting transpressional regime was responsible for most of the exhumation of high-grade metamorphic rock units with initial increasing temperature followed by decompression and cooling [Carosi et al., 2009, Di Vincenzo et al., 2004]. In the HGMC, two opposite senses of shear (top to the NW and top to the SE/NE) on the S2 foliation have been interpreted by Corsi and Elter [2006] as being associated with the end of compression/crustal thickening (the first, top to the NW) and with tectonic inversion during the exhumation of the metamorphic basement (top to the SE/NE). D3 deformation is characterized mainly by metric chevron and/or asymmetric folds associated with an S3 axial plane crenulation cleavage. The D4 tectonic phase forms metric to decametric-scale folds with subhorizontal axial planes. It is not associated with the development of foliations and object lineations. The metamorphic basement of Sardinia was finally intruded by the Permo–Carboniferous batholith emplaced between ~320 and 280 Ma [Carmignani et al., 2001, Casini et al., 2015, and references therein].

3. Field geology

The study area is located in the Posada Valley, in the northernmost part of the L-MGMC, along the PASZ (Figure 1). In this area, from Punta Figliacoro to Pedra su Gattu, the metamorphic complex consists of metabasite, orthogneiss, paragneiss, mylonite, and micaschist (Figure 1(b)). The metabasites, known in literature as the Posada amphibolites [Carosi and

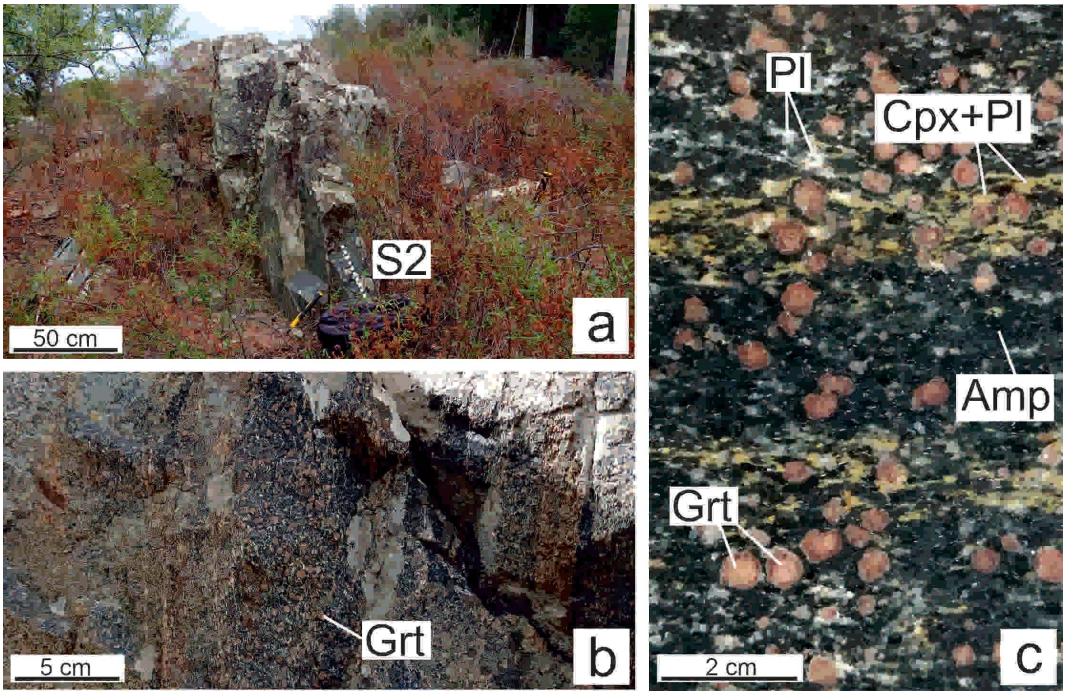

Figure 2. Amphibolites from Pedra su Gattu locality: (a) field aspect of the amphibolites; at the outcrop scale, the rocks show an S2 regional foliation (dotted line); (b) detail of a garnet-rich layer in the amphibolites; (c) cut and polished hand sample from garnet-rich layer; Grt = garnet; Pl = plagioclase; Cpx = clinopyroxene; Amp = amphibole.

Elter, 1989], outcrop as bodies and/or lenses ca. 300 m long and 100 m wide within the mylonites. These lenses follow a W–E direction (Figure 1(b)) and corresponds to small hills inside the valley, due to their higher resistance to erosion as compared to the surrounding mylonites. The geological and structural relationships between the different rocks cropping out in the Posada Valley had been described since Elter et al. [1990, their Figure 7, p. 398]. The metabasites at Pedra su Gattu are slightly foliated rocks characterized by an irregular and discontinuous alternance of garnet-rich and garnet-poor layers (Figure 2). The most foliated portions display dark-green, amphibole-rich layers alternating with whitish, plagioclase-rich ones. Garnet porphyroblasts (up to a maximum of 1–2 cm in size) are observed in both layers (Figure 2(b)). Locally, inside the amphibole-rich bands, discontinuous millimetric to centimetric-thick layers with a yellowish clinopyroxene + plagioclase assemblage can be observed. These layers, as well as the amphibole- and plagioclase-rich bands, are parallel to the S2 regional foliation (Figure 2(c)).

The mylonitized schist and gneiss that surround the metabasite bodies derive from igneous and sedimentary protoliths which underwent intense deformation and shearing. They show a prominent planar anisotropy that results in a penetrative schistosity in which the only visible mineral is muscovite or, more rarely, biotite.

4. Analytical methods

An FEI Quanta 200 scanning electron microscope (SEM), equipped with a nitrogen free Thermofisher EDS-X-ray detector at Centro Servizi d'Ateneo per la Ricerca (CeSAR) of Cagliari University, was used for microstructural investigation. Mineral chemistry was determined with a fully automated JEOL 8200 Super Probe at Dipartimento di Scienze della Terra

"Ardito Desio", Università di Milano. Operating conditions were 15 kV accelerating voltage, beam current of 15 nA, and 5–10 μm variable spot size. Natural and synthetic wollastonite, olivine, corundum, magnetite, rutile, orthoclase, jadeite, pure Mn, pure Cr, fluorophlogopite, and barite were used as standards. Selected samples were cut in thin slices and then pulverized for major elements whole-rock analyses, which were performed at ALS-Laboratories (Seville) by X-ray fluorescence (XRF) after lithium-borate fusion. *P*–*T* pseudosections were calculated using the software package PERPLE_X [Connolly, 1990, 2009] and the thermodynamic data set of Holland and Powell [1998, updated 2011] for H_2O and minerals.

5. Petrography

Four samples from Pedra su Gattu area were selected: two garnet-rich amphibolites (U1 and U4), and two garnet-poor amphibolites (U5 and U33), the latter two representing retrogressed domains. Garnet-rich samples (U1, U4) are characterized by the presence of subhedral to euhedral porphyroblastic garnet (Figures 2(c), 3(a)). The garnet porphyroblasts are occasionally concentrated along layers parallel to the main foliation in the amphibolites. Garnet contains several inclusions of epidote (Ep_{1a}), titanite (Ttn_{1a}), quartz, and euhedral grains of amphibole (Amp_{1a}) and plagioclase (Pl_{1a}) (Figures 3(b, c)), mostly concentrated in the garnet core (Figure 3(a)). Trace amounts of clinopyroxene (Cpx_{1a}) have also been found as inclusions in garnet. Chlorite can occur as a filling phase mineral inside the cracks. Garnet porphyroblasts are surrounded by a sub-millimetric thin rim of plagioclase (Pl_{2a}), commonly sericitized, and minor amphibole (Amp_{2a}) (Figure 3(d)). The rock matrix is mainly made up of anhedral crystals of amphibole (Amp_{2b}) and plagioclase (Pl_{2b}) and small flakes or trails of fine-grained clinopyroxene (Cpx_{1b}) and plagioclase (Pl_{1b}) (±amphibole; Amp_{1b}), elongated parallel to the regional schistosity (Figures 3(e, f)). Plagioclase from the matrix (Pl_{2b}) can be arranged in trails of coarse-grained crystals along the S2 foliation. Amphibole from the matrix (Amp_{2b}) is locally and partially replaced with a late-stage amphibole (actinolite, Amp_3). In the proximity of garnet, the elongation of amphibole follows the direction of garnet edges. The rock matrix contains abundant titanite (Ttn_{2b}, up to 3 mm in size), occasionally in association with ilmenite, and, more rarely, with albite. Other minerals in the matrix are epidote, quartz, chlorite, apatite, prehnite, biotite, and trace amounts of rutile and K-feldspar. Zircon is accessory mineral. The garnet-poor samples (U5 and U33) are characterized by abundant amphibole and plagioclase oriented parallel to the regional S2 schistosity. Rare garnet relics are replaced by amphibole and chlorite. Other minerals observed are epidote, titanite, quartz, very rare biotite, and ilmenite.

The metamorphic evolution of the Posada Valley amphibolites is summarized in Figure 4. The early history recorded by the amphibolites is linked to the growth of garnet porphyroblasts and its inclusions (stage 1a) and the formation of the Cpx_{1b} + Pl_{1b} (±Amp_{1b}) mineral assemblage (stage 1b). The minerals around garnet (Amp_{2a} + Pl_{2a}; stage 2a) and the mineral assemblage in the rock matrix (mostly Amp_{2b} + Pl_{2b}; stage 2b) represent the subsequent retrograde re-equilibration. The last metamorphic stage (stage 3) is related to the local growth of late retrograde phases such as actinolite, chlorite, albite, titanite. Prehnite is ascribed to sub-greenschists facies stage.

6. Mineral chemistry

Selected microprobe analyses of garnet, clinopyroxene, amphibole, plagioclase, epidote, and titanite from samples U1 and U4 and from retrogressed samples U5 and U33 of the Posada Valley amphibolites are reported in Tables 1–3 and S1 of Supplementary Material.

The garnet composition, in terms of molar fractions, is $Alm_{0.49–0.54}Grs_{0.34–0.42}Prp_{0.07–0.11}Sps_{0.01–0.05}$ (with components Alm: almandine, Grs: grossular [+andradite], Prp: pyrope, Sps: spessartine). Compositional X-ray maps (Mg, Fe, Ca, Mn) of two selected garnet crystals from samples U1 and U4 are shown in Figure 5. Garnet porphyroblasts show a weak compositional zoning, graphically represented in the compositional rim–core–rim profiles reported in Figure 6. By using the molar content of Ca (garnet core = $X_{Ca} < 0.40$; garnet mantle = $X_{Ca} > 0.40$; garnet rim = $X_{Ca} < 0.40$) as a reference, we distinguished three compositional garnet domains: a core, a mantle, and a rim (Figures 5, 6). The representative garnet core composition is $Alm_{0.51–0.53}Grs_{\sim 0.35}Prp_{\sim 0.10}Sps_{0.03}$.

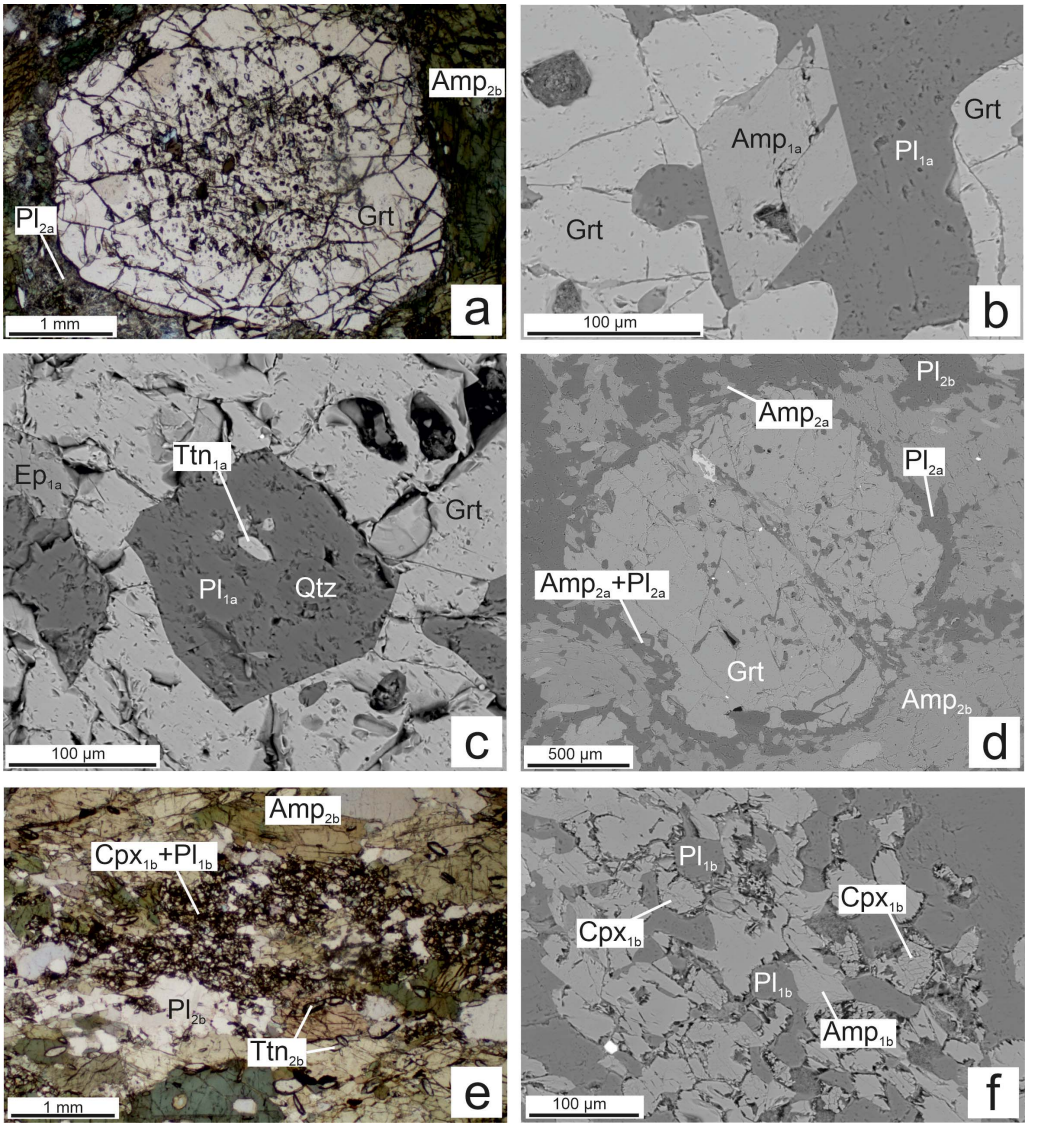

Figure 3. Photomicrographs showing the most relevant microstructural features of the amphibolites from Pedra su Gattu. (a) Overview of a garnet porphyroblast with several inclusions concentrated in the core, plane polarized light; sample U1; (b) BSE image of euhedral amphibole in garnet (sample U1); (c) BSE image of plagioclase inclusion in garnet. The plagioclase inclusion in turn contains titanite and quartz nanoinclusions (sample U4); (d) BSE image of the $Pl_{2a} + Amp_{2a}$ rim around garnet; sample U1; (e) overview of the matrix containing elongated flakes of $Cpx_{1b} + Pl_{1b}$; plane polarized light; sample U4; (f) BSE image showing a detailed view of $Cpx_{1b} + Pl_{1b}$ ($\pm Amp_{1b}$), sample U1.

From core to mantle almandine decreases down to 49 mol% and then slightly increases towards the rim (51 mol%). Grossular shows a moderate increase from core to mantle (up to 41–42 mol%) and a faint decrease down to 38–39 mol% in the rim. Pyrope keeps an almost constant concentration through the rim–core–rim profile with a very slight decrease in the mantle (down to 7 mol%). Spessartine very slightly decreases to 1–2 mol% in the rim. Garnet compositional zoning of the Posada Val-

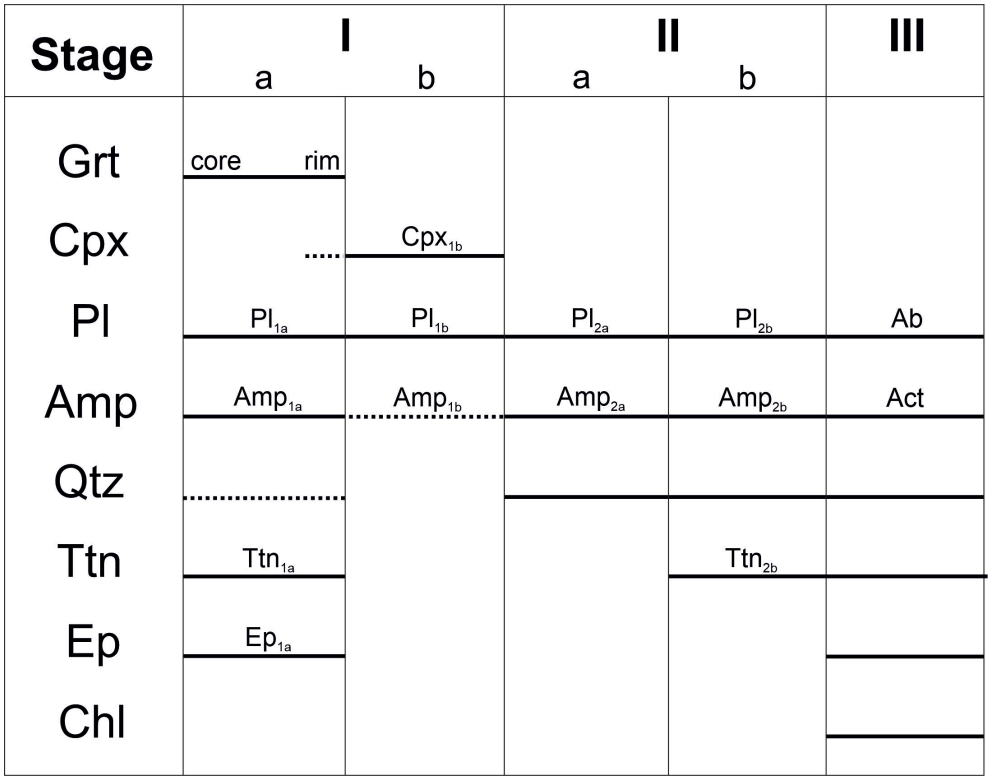

Figure 4. Metamorphic evolution scheme deduced from microtextural observation and analyses of amphibolites from Pedra su Gattu locality. Mineral abbreviations as in Figure 2. Qtz = quartz; Ttn = titanite; Ep = epidote; Chl = chlorite; Ab = albite; Act = actinolite.

ley amphibolites resemble that of the retrogressed eclogites from the L-MGMC [Cruciani et al., 2015c] and differs from that of the HGMC eclogites [Cruciani et al., 2019].

Plagioclase inclusions in garnet (Pl_{1a}) are oligoclase with X_{Na}[=Na/(Na+Ca)] values of 0.87–0.88. Pl_{1b} ranges between andesine and oligoclase with X_{Na} in the range 0.64–0.84. Pl_{2a} and Pl_{2b} both show a wide compositional range from andesine to albite (X_{Na} = 0.57–0.91; X_{Na} = 0.51–0.92, respectively). In the most retrogressed samples (U5, U33) X_{Na} values show a narrower range of 0.68–0.75. Late-stage plagioclase (Ab) is albite (X_{Na} = 0.91–0.93).

All the analysed amphiboles are calcic according to the amphibole supergroup classification IMA 2012 [Hawthorne et al., 2012] (Figure 7). Amp_{1a} is pargasite or Fe-pargasite with Si = 6.5 atoms per formula unit (apfu) and X_{Mg}[=Mg/(Mg+Fe^{2+})] = 0.53–0.61. Amp_{1b} is pargasite with Si = 6.4–6.5 apfu and X_{Mg} ratio of 0.52–0.60. Amp_{2a} is pargasite or Fe-pargasite with Si content ranging from 6.2 to 6.5 apfu and X_{Mg} = 0.45–0.56. Amp_{2b} is pargasite/Fe-pargasite to Mg-hornblende, with Si = 6.3–7.1 apfu and X_{Mg} = 0.48–0.62. Amp_3 is actinolite with Si = 7.6–7.7 apfu and X_{Mg} around 0.64–0.72. Cpx_{1b} is diopside with X_{Na} and X_{Mg} ratios of 0.04–0.08 and 0.66–0.72, respectively (Figure 8).

Epidote in garnet (Ep_{1a}) is characterized by a variable trivalent iron content ranging from 0.15 to 1.00 apfu. Titanite inclusions and matrix titanite do not show significant differences in composition.

7. Pressure–temperature evolution

7.1. *Isochemical phase diagram*

The metamorphic history of the Posada Valley amphibolites has been reconstructed by *P*–*T* pseudosections in the NCKFMASHO+Ti+Mn system calculated in the range 400–800 °C, 0.2–1.8 GPa for

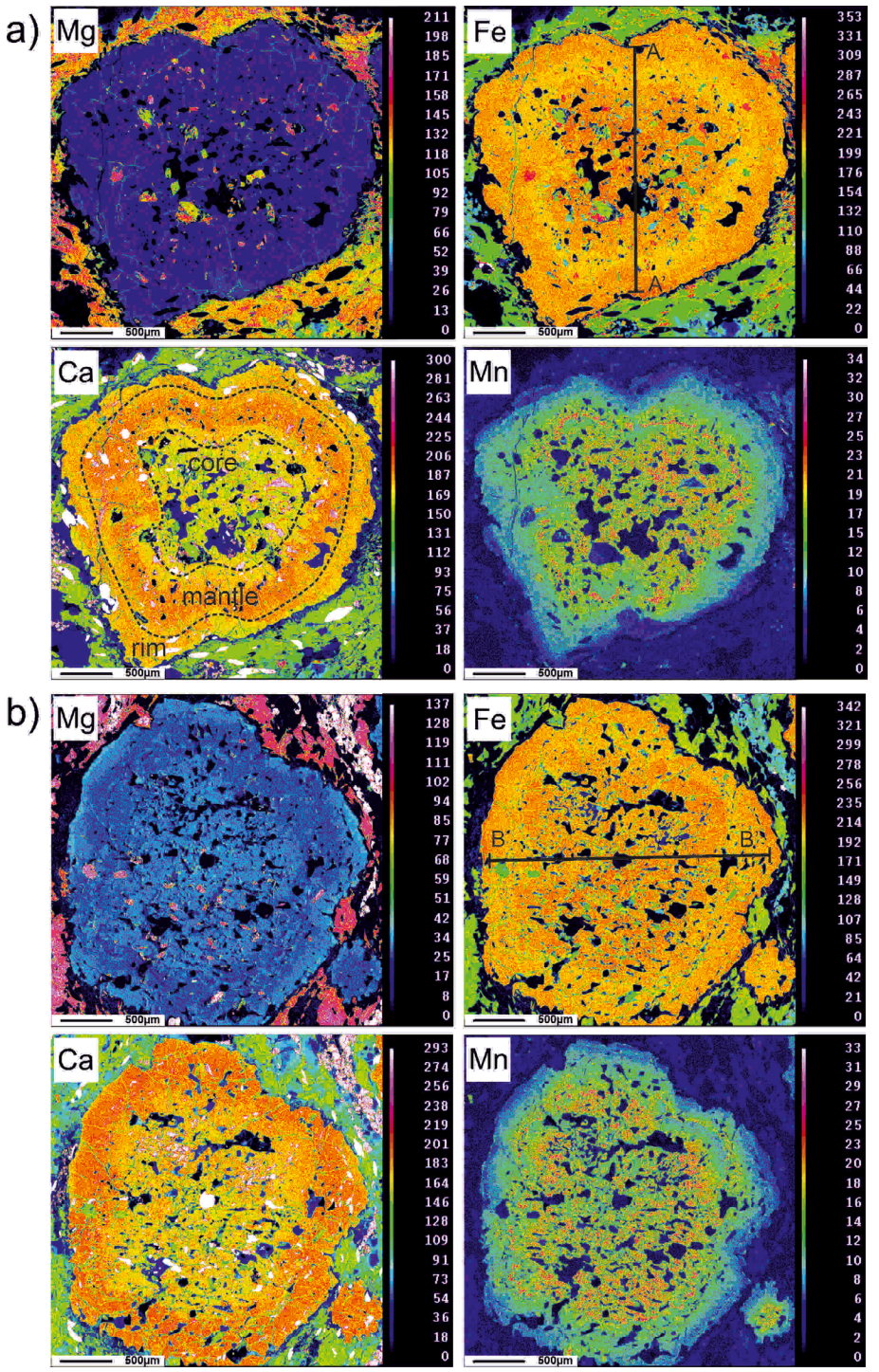

Figure 5. Mg, Fe, Ca, and Mn concentration maps of a selected garnet crystal from (a) sample U1 and (b) sample U4. The scales for the colour code on the right-hand side of each image indicate counts of specific X-ray radiation per time unit.

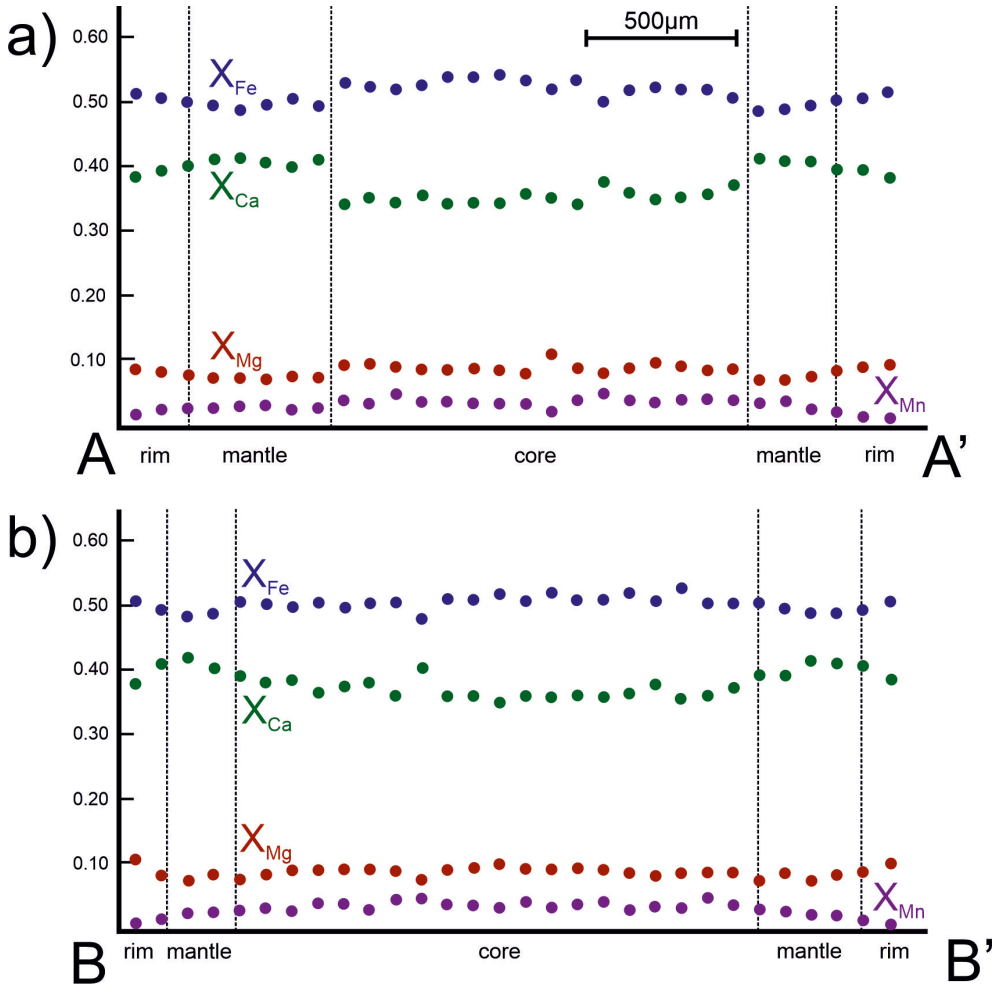

Figure 6. Rim–core–rim compositional profiles of the garnet crystals from samples (a) U1 and (b) U4, along the lines A–A′ and B–B′ shown in Figure 5. Element concentrations are expressed in molar fractions.

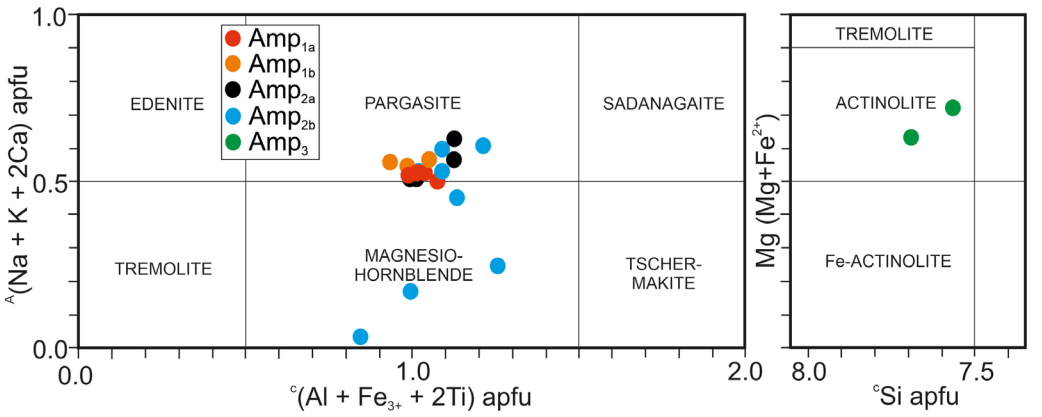

Figure 7. Ca–amphibole classification IMA 2012 [Hawthorne et al., 2012] for the Posada Valley amphibolites.

Table 1. Representative microprobe analyses of garnet and clinopyroxene from samples U1, U4

	U1			U4			U1	U4
	Grt_{core}	Grt_{mantle}	Grt_{rim}	Grt_{core}	Grt_{mantle}	Grt_{rim}	Cpx_{1b}	Cpx_{1b}
SiO_2	38.39	38.81	38.49	38.61	38.79	39.04	54.40	53.75
TiO_2	0.37	0.08	0.11	0.29	0.07	0.04	0.08	0.09
Al_2O_3	21.25	21.82	21.39	21.39	21.82	21.97	1.38	1.16
Cr_2O_3	0.10	0.03	0.03	—	0.02	—	—	—
Fe_2O_3	0.72	0.31	0.67	0.83	0.39	0.27	—	—
FeO	24.41	22.53	24.07	23.52	22.33	23.54	8.94	9.74
MnO	1.51	1.28	0.79	1.49	1.16	0.40	0.07	0.09
MgO	2.25	1.91	2.30	2.68	1.94	2.82	12.57	12.38
CaO	12.48	15.11	14.14	12.81	15.36	13.90	23.24	23.42
Na_2O	—	—	—	—	—	—	0.71	0.72
Total	101.48	101.88	101.99	101.62	101.88	101.98	101.39	101.35
Oxygen	24	24	24	24	24	24	6	6
Si	5.97	5.98	5.95	5.98	5.98	5.98	2.00	1.99
Ti	0.04	0.01	0.01	0.03	0.01	0.00	0.00	0.00
Al	3.90	3.97	3.90	3.90	3.96	3.97	0.06	0.05
Cr	0.01	0.00	0.00	—	0.00	—	—	—
Fe^{3+}	0.08	0.04	0.08	0.10	0.05	0.03	—	—
Fe^{2+}	3.18	2.91	3.11	3.05	2.87	3.02	0.27	0.30
Mn	0.20	0.17	0.10	0.20	0.15	0.05	0.00	0.00
Mg	0.52	0.44	0.53	0.62	0.44	0.64	0.69	0.68
Ca	2.08	2.49	2.34	2.13	2.53	2.28	0.91	0.93
Na	—	—	—	—	—	—	0.05	0.05
X_{Na}	—	—	—	—	—	—	0.05	0.05
X_{Mg}	—	—	—	—	—	—	0.71	0.69
Alm	0.53	0.48	0.50	0.51	0.48	0.50	—	—
Prp	0.09	0.07	0.09	0.10	0.07	0.11	—	—
Grs	0.35	0.42	0.39	0.35	0.42	0.38	—	—
Sps	0.03	0.03	0.02	0.03	0.03	0.01	—	—

the bulk composition of samples U1, U4, and U5, U33 (Pedra su Gattu locality). The used solid solution models are those of Holland and Powell [1998] for garnet, white mica, Holland and Powell [2011] epidote, Holland and Powell [1996] orthopyroxene, Green et al. [2007] clinopyroxene, Holland et al. [1998] chlorite, Powell and Holland [1999] biotite, Dale et al. [2005] amphibole, White et al. [2000, 2014] ilmenite, and Benisek et al. [2010] for plagioclase. All pseudosections were calculated considering H_2O as a saturated component. On the basis of the mode and composition of Fe^{3+}-rich minerals (epidote, amphibole), abundant in the rock matrix and as inclusions in garnet, 10% of trivalent iron (corresponding to ca. 0.15 wt% of O_2) has been chosen. We did not noticed significant differences in the topology of the *P*–*T* field of interest, nor in the geothermobarometric results, for *P*–*T* pseudosection calculations with lower (5%) trivalent iron. The bulk–rock composition used to calculate *P*–*T* conditions for metamorphic stage 1 (garnet core) was obtained by XRF analyses corrected for apatite and normalized

Table 2. Representative microprobe analyses of amphibole from samples U1, U4, U5, and U33

	U1					U4					U5	U33
	Amp1a	Amp1b	Amp2a	Amp2b	Amp3	Amp1a	Amp1b	Amp2a	Amp2b	Amp3	Amp2b	Amp2b
SiO_2	44.68	44.77	42.54	45.50	51.18	44.68	44.25	44.46	44.29	53.45	49.98	49.15
TiO_2	0.87	1.07	0.79	0.85	0.06	0.64	0.68	0.42	0.78	0.11	0.77	0.92
Al_2O_3	11.40	11.66	14.14	12.29	2.67	12.42	12.61	12.18	11.99	2.20	9.67	12.95
Cr_2O_3	0.01	0.06	0.18	0.03	0.07	—	0.07	0.09	0.09	0.02	—	—
Fe_2O_3	6.69	3.63	4.99	2.46	3.77	5.74	3.49	4.31	4.32	2.09	2.52	—
FeO	14.33	13.15	14.13	13.08	10.37	11.94	14.81	13.97	14.57	13.77	12.92	12.72
MnO	0.17	0.10	0.19	0.11	0.11	0.06	0.23	0.16	0.17	0.40	—	—
MgO	8.94	10.87	8.66	10.88	14.63	10.33	9.31	9.78	9.50	13.93	11.61	11.10
CaO	11.25	11.99	11.55	12.00	12.15	11.22	11.83	11.91	11.84	12.60	11.15	10.78
Na_2O	1.81	1.82	2.05	1.59	0.27	1.99	1.77	1.71	1.75	0.31	1.64	1.75
K_2O	0.45	0.48	0.57	0.50	0.07	0.47	0.56	0.49	0.53	0.10	—	0.62
H_2O	2.06	2.05	2.04	2.07	2.03	2.07	2.05	2.05	2.05	2.08	1.98	1.99
Total	102.66	101.65	101.83	101.36	97.38	101.56	101.66	101.53	101.88	101.06	102.24	101.98
Oxygen	23	23	23	23	23	23	23	23	23	23	23	23
Si	6.51	6.51	6.24	6.59	7.57	6.49	6.48	6.51	6.48	7.69	7.06	6.92
Al^{IV}	1.49	1.49	1.76	1.41	0.43	1.51	1.52	1.49	1.52	0.31	0.94	1.08
Al^{VI}	0.46	0.51	0.69	0.69	0.04	0.61	0.65	0.61	0.55	0.07	0.68	1.07
Ti	0.09	0.12	0.09	0.09	0.01	0.07	0.07	0.05	0.09	0.01	0.08	0.10
Cr	0.00	0.01	0.02	0.00	0.01	—	0.01	0.01	0.00	0.00	—	—
Fe^{3+}	0.73	0.40	0.55	0.27	0.42	0.63	0.38	0.47	0.48	0.23	0.27	—
Fe^{2+}	1.75	1.60	1.73	1.58	1.28	1.45	1.81	1.71	1.78	1.66	1.53	1.50
Mn	0.02	0.01	0.02	0.01	0.01	0.01	0.03	0.02	0.02	0.05	—	—
Mg	1.94	2.36	1.89	2.35	3.23	2.24	2.03	2.13	2.07	2.99	2.45	2.33
Ca	1.76	1.87	1.82	1.86	1.93	1.75	1.86	1.87	1.86	1.94	1.69	1.63
Na	0.51	0.51	0.58	0.45	0.08	0.56	0.50	0.49	0.50	0.09	0.45	0.48
K	0.08	0.09	0.11	0.09	0.01	0.09	0.10	0.09	0.10	0.02	—	0.11
H	2.00	2.00	2.00	2.00	2.00	2.00	2.00	2.00	2.00	2.00	2.00	2.00
X_{Mg}	0.53	0.60	0.52	0.60	0.72	0.61	0.53	0.56	0.54	0.64	0.62	0.61
	Fe-parg.	parg.	Fe-parg.	Mg-hbl.	act.	parg.	parg.	parg.	parg.	act.	Mg-hbl.	Mg-hbl.

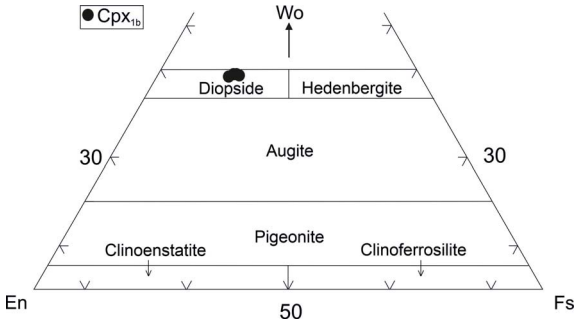

Figure 8. Clinopyroxene (Cpx_{1b}) classification in the Wo–En–Fs diagram.

to 100% (Table 4). The resulting *P*–*T* pseudosection for sample U1 is shown in Figure 9(a). The main stage 1 phases (garnet, clinopyroxene, amphibole, and plagioclase) are stable in the multivariant *P*–*T* fields at <1.0–1.1 GPa, <600 °C. Further constrains on stage I have been obtained by garnet core and garnet rim composition. Figure 9(b) shows the intersection of almandine (X_{Fe} = 0.53), grossular (X_{Ca} = 0.33), pyrope (X_{Mg} = 0.10), and spessartine (X_{Mn} = 0.03) for garnet core composition, and of X_{Ca}[=Ca/(Ca+Na)]= 0.12–0.14 for Pl_{1a}. In addition, the isomodes 15 and 20 vol.% for garnet were drawn, which represent the maximum amount observed in the sample. All these isopleths and isomodes cross or come close together

Table 3. Representative microprobe analyses of plagioclase from samples U1, U4, U5, and U33

	U1				U4					U5	U33
	Pl_{1a}	Pl_{1b}	Pl_{2a}	Pl_{2b}	Pl_{1a}	Pl_{1b}	Pl_{2a}	Pl_{2b}	Ab	Pl_{2b}	Pl_{2b}
SiO_2	66.24	65.42	67.00	62.18	66.18	62.25	60.81	66.00	66.88	64.46	61.90
TiO_2	0.03	—	—	—	0.03	0.03	—	—	0.04	—	—
Al_2O_3	21.15	22.05	21.02	24.45	21.50	24.01	25.86	20.85	20.40	23.10	24.53
Fe_2O_3	0.15	0.21	0.32	0.23	0.21	0.20	0.27	0.10	0.02	—	—
CaO	2.40	3.29	2.09	5.81	2.72	5.59	5.67	2.45	1.70	4.98	6.34
Na_2O	10.08	9.89	10.57	8.43	10.24	8.56	7.38	10.10	10.96	7.46	7.23
K_2O	0.10	0.16	0.08	0.12	0.05	0.13	0.80	0.10	0.11	—	—
Total	100.16	101.01	101.08	101.23	100.97	100.78	100.79	99.60	100.14	100.00	100.00
Oxygen	8	8	8	8	8	8	8	8	8	8	8
Si	2.90	2.86	2.91	2.73	2.89	2.74	2.68	2.91	2.93	2.83	2.74
Ti	0.00	—	—	—	0.00	0.00	—	—	0.00	—	—
Al	1.09	1.13	1.08	1.27	1.10	1.25	1.34	1.08	1.05	1.19	1.28
Fe^{3+}	0.01	0.01	0.01	0.01	0.01	0.01	0.01	0.00	0.00	—	—
Ca	0.11	0.15	0.10	0.27	0.13	0.26	0.27	0.12	0.08	0.23	0.30
Na	0.86	0.84	0.89	0.72	0.87	0.73	0.63	0.86	0.93	0.63	0.62
K	0.01	0.01	0.00	0.01	0.00	0.01	0.04	0.01	0.01	—	—
X_{Na}	0.88	0.84	0.90	0.72	0.87	0.73	0.70	0.88	0.92	0.73	0.67
X_{Ca}	0.12	0.16	0.10	0.28	0.13	0.27	0.30	0.12	0.08	0.27	0.33

at conditions of P = 0.9–1.2 GPa and T = 530–620 °C (Figure 9(b)). The fields with plagioclase + garnet + biotite + clinopyroxene + amphibole + chlorite ± titanite ± rutile ± ilmenite ± epidote ± quartz matches the mineralogical composition of the sample. P–T conditions obtained with the same approach for sample U4 are 1.0–1.3 GPa and 550–650 °C (Figure S1a, b, in Supplementary Material).

For the P–T conditions of the garnet rim, an effective composition was obtained by subtracting the garnet core and mantle from the bulk–rock composition after considering the garnet mode in the rock (15%) and the volume area of the core and mantle estimated from the X-ray maps (by using an image analysis software) and EMP analyses (core+mantle around 60% in both U1 and U4 samples). The resulting P–T pseudosection is shown in Figure 9(c). The selected isomodes (15–20 vol.%) and isopleths of garnet (X_{Mg} = 0.10), plagioclase (Pl_{1a}/Pl_{1b} X_{Ca} = 0.14–16), clinopyroxene (Cpx_{1b} X_{Mg} = 0.66–68) constrain P–T conditions at 1.0–1.4 GPa and 590–690 °C (Figure 9(d)). Garnet isomode trend evidences a slight, prograde increase in temperature and pressure with garnet growth. The corresponding stability fields (clinopyroxene + plagioclase + amphibole + garnet + biotite ± ilmenite ± chlorite ± rutile) match the mineral assemblage observed in the rock samples. Similar P–T conditions have been obtained with the same approach for sample U4 (1.0–1.3 GPa and 570–680 °C; Figure S1c, d).

In order to gain P–T conditions for metamorphic stage 2, the composition of the most retrogressed samples at Pedra su Gattu locality (U5 and U33, Table 4), with abundant amphibole and plagioclase (i.e., Amp_{2b} and Pl_{2b}) was used. The resulting P–T pseudosection for sample U5 is shown in Figure 9(e). Amphibole and plagioclase display a large stability field at high temperatures and low pressures (Figure 9(e)). Figure 9(f) shows the intersection, for sample U5, of isopleths for the Si content (Si = 7.0–7.1 apfu) and X_{Mg} (0.62) in Amp_{2b} with X_{Ca} = 0.28 of Pl_{2b}. Lower temperatures of ca. 50 °C are obtained by calculations with all divalent iron (dotted green line in Figure 9). The resulting P–T conditions are P = 0.5–0.8 GPa and T = 600–700 °C (marked by the ellipse in Figure 9(f)). These condi-

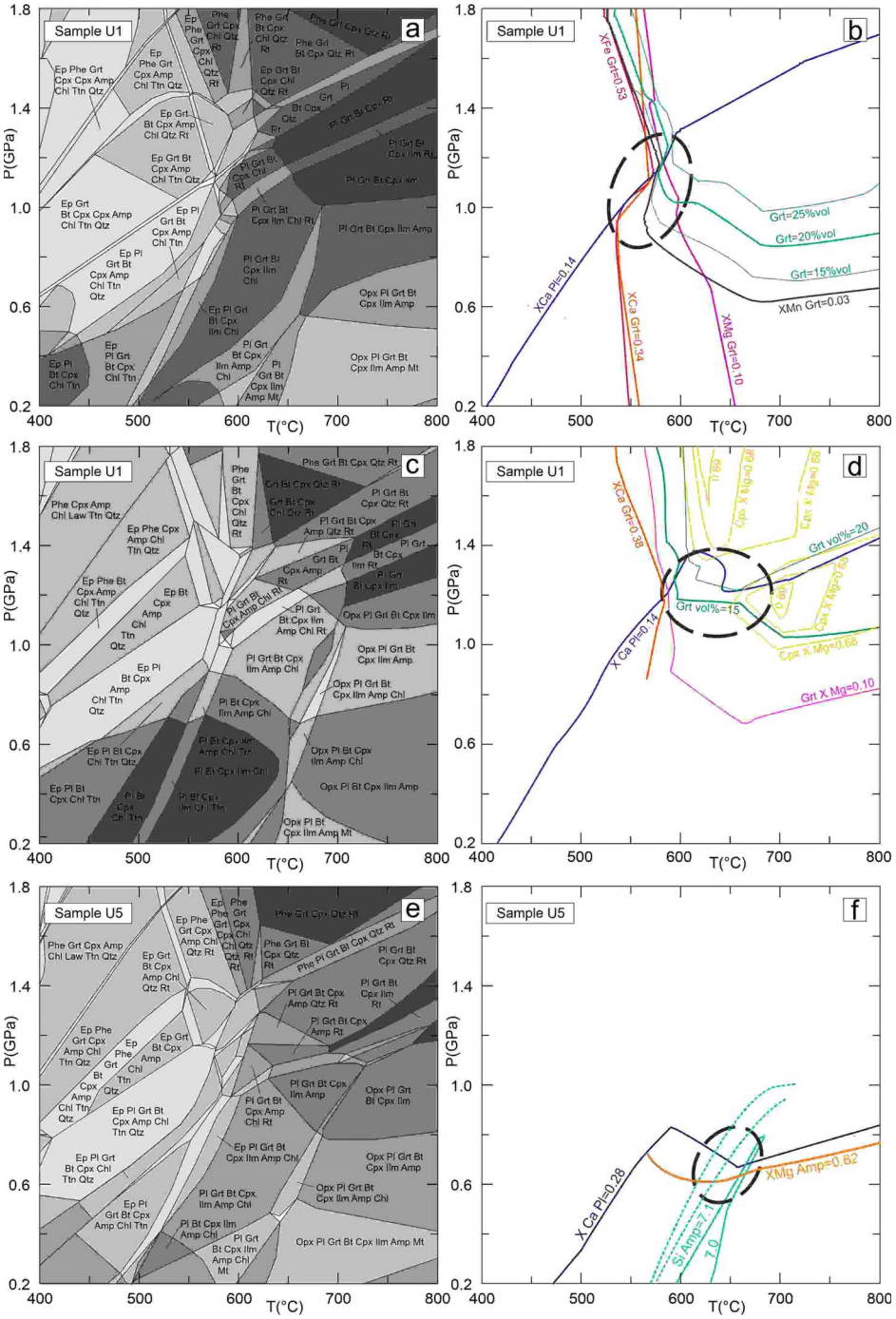

Figure 9. *P–T* pseudosection (a) and selected compositional isopleths for garnet and plagioclase (b) for the bulk composition of sample U1; *P–T* pseudosection (c) and selected compositional isopleths for garnet and plagioclase (d) for the bulk composition of sample U1 minus the composition of garnet core+mantle; *P–T* pseudosection (e) and selected compositional isopleths for amphibole and plagioclase (f) for the bulk composition of re-equilibrated sample U5. Dotted green lines represent amphibole Si (apfu) isopleths calculated with all divalent iron in the bulk composition.

Table 4. Bulk–rock analyses (wt%) of samples U1, U4, U5, and U33 determined by X-ray fluorescence (XRF) spectrometry and modified compositions for the calculation of *P*–*T* pseudosections (see text for details)

	U1			U4			U5		U33	
	XRF	Bulk core	Bulk rim	XRF	Bulk core	Bulk rim	XRF	Bulk	XRF	Bulk
SiO_2	47.64	48.48	51.17	48.36	49.55	52.2	50.15	50.88	49.94	50.92
TiO_2	1.88	1.91	2.27	1.77	1.81	2.15	1.47	1.49	1.35	1.38
Al_2O_3	14.06	14.31	13.15	15.05	15.42	14.4	14.58	14.79	16.03	16.35
Fe_2O_3	14.51	—	—	13.52	—	—	12.43	—	11.56	—
FeO_{tot}	—	13.29	11.52	—	12.47	10.52	—	11.34	—	10.61
MgO	6.09	6.2	7.1	5.29	5.42	6.1	5.87	5.96	5.53	5.64
MnO	0.21	0.21	0	0.24	0.25	0.05	0.18	0.18	0.18	0.18
CaO	10.54	10.45	9.92	10.36	10.3	9.63	9.49	9.42	10.14	10.15
Na_2O	3.54	3.6	4.35	3.78	3.87	4.65	3.99	4.05	3.77	3.84
K_2O	0.43	0.44	0.53	0.66	0.24	0.29	0.72	0.73	0.77	0.79
P_2O_5	0.21	—	—	0.23	—	—	0.16	—	0.14	—
O_2	—	0.15	0.13	—	0.17	0.16	—	0.13	—	0.12

Bulk core: composition for modelling the garnet core obtained by XRF analyses corrected for apatite and normalized to 100%. Bulk rim: effective composition for modelling the garnet rim obtained by subtracting the garnet core and mantle from the bulk–rock composition.

tions overlap two stability *P*–*T* fields which differ for the presence/absence of chlorite, ilmenite, and orthopyroxene (clinopyroxene + plagioclase + amphibole + garnet + biotite ± ilmenite ± chlorite ± orthopyroxene). Except for titanite (observed in the rock instead) and orthopyroxene (not present), the assemblage corresponds to what is observed in the sample. Similar results have been obtained with the same method on sample U33 (Figure S1e, f). Temperature estimates on the same amphibole–plagioclase pairs by the Holland and Blundy [1994] and Blundy and Holland [1990] geothermometers are in the range 580–640 °C and 560–650 °C for samples U5 and U33, respectively.

8. Discussion

8.1. *P–T evolution of the Posada Valley amphibolites*

The Posada Valley amphibolites recorded three stages of metamorphic evolution (Figure 10): (1) prograde evolution from 0.9–1.2 GPa and T = 530–620 °C to HP conditions at 1.0–1.4 GPa and 590–690 °C; (2) a retrograde stage documented by matrix phases, characterized by an almost isothermal decompression from stage I (with a very slight increase in temperature) down to P = 0.5–0.8 GPa and T = 600–700 °C; and (3) the local growth of late phases such as actinolite, chlorite, and epidote which overgrew or replaced minerals of the previous stages (about P = 0.2–0.3 GPa and T = 330–350 °C), as already documented for several metabasites from NE Sardinia [Franceschelli et al., 2007, Cruciani et al., 2012]. Further re-equilibration in sub-greenschist facies is suggested by the occurrence of prehnite. The resulting *P*–*T* path is clockwise (Figure 10).

The Posada Valley amphibolites reached peak–pressure conditions up to 1.4 GPa, at transitional *P*–*T* conditions between amphibolite, HP granulite, and amphibole–eclogite facies fields. These rocks never fully reached eclogite facies conditions, according to the following two observations: (1) in the large amount of observed samples, no omphacite relics were found, neither as inclusion in garnet porphyroblasts; (2) plagioclase occurs in every stage of the metamorphic evolution, primarily as inclusion in garnet as documented in the petrographic description and in Figures 3(b, c).

The *P*–*T* path is consistent with those of other

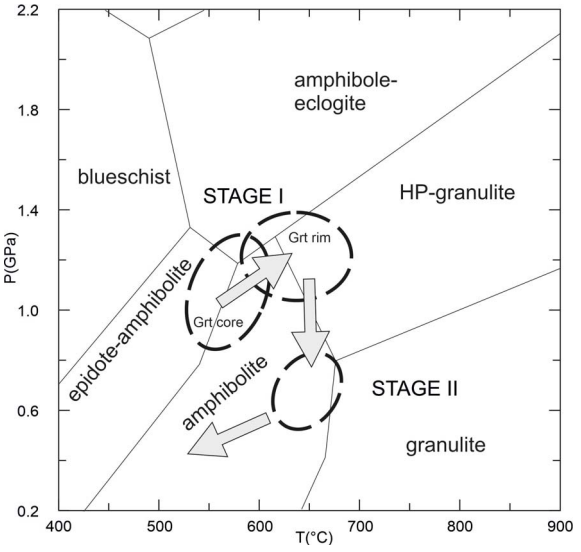

Figure 10. *P*–*T* path for the Posada Valley amphibolites (arrows). Facies field areas from Liou et al. [1998].

metabasites and metamorphic rocks from the inner zone of the Sardinian basement, with the exception of the Mt. Nieddu banded and ultrabasic amphibolites [Scodina et al., 2019, 2020, Cruciani et al., 2020] which recorded instead an anticlockwise *P*–*T* evolution.

For a thorough comparison of the *P*–*T* history and evolution of metamorphic rocks belonging to the northern part of the medium-grade metamorphic complex, nearby the PASZ, such as the Giuncana eclogites [Cruciani et al., 2015a] and retrogressed eclogites of the Migmatite complex the reader is referred to Cruciani et al. [2011, 2015c]. The Giuncana eclogites, belonging to the medium-grade metamorphic complex, experienced a clockwise *P*–*T* path divided in four metamorphic stages: from an HP stage at 580 < *T* < 660 °C, 1.3 < *P* < 1.8 GPa, the eclogite underwent pressure decrease and temperature increase, leading to the breakdown of omphacite at ~1.25–1.40 GPa and 650–710 °C. The subsequent amphibolite facies re-equilibration occurred at *T* = 600–670 °C, *P* = 0.65–0.95 GPa, and subsequently, in the range of greenschist facies conditions. The shape of the resulting *P*–*T* trajectory [Figure 11, p. 810 of Cruciani et al., 2015c] is similar to the path reconstructed for the here studied Posada Valley amphibolites. However, the pressure peak is fairly different (lower) and this resulted in different petrographic features.

Retrogressed eclogites of the Migmatite complex (Punta de Li Tulchi, Golfo Aranci, Punta Tittinosu) experienced an eclogite facies stage at 1.6–2.1 GPa, 660–700 °C, followed by granulite facies equilibration with temperature in excess of 800 °C and pressure in the range of 1.0–1.3. These stages were in turn followed by re-equilibration into low-*P* amphibolite facies and greenschist facies. The studied amphibolites from Posada Valley, similarly to the other metabasites from the L-MGMC, underwent a cooler evolution, predating the Barrovian stage, with a thermal peak lower than that recorded by the eclogites embedded in HGMC.

8.2. *Geodynamic scenario*

The Variscan collisional geodynamic scenario for southern Corsica and northern Sardinia has been depicted in a couple of recent papers [Scodina et al., 2019, Cruciani et al., 2021]. This scenario comprises the presence of metamorphic rocks with clockwise and anticlockwise *P*–*T* path coupled together within the inner zone of the Variscan chain in northern Sardinia and southern Corsica [Massonne et al., 2018, Scodina et al., 2019, 2020, Cruciani et al., 2021]. The geodynamic models proposed by these authors provide the presence of rock slices from different crustal levels of both upper and lower continental plates that were involved in collisional tectonics and subsequently brought adjacent to each other during the uplift in an exhumation channel [Massonne, 2016]. According to Massonne [2012], an exhumation channel is an environment in which, in spite of an upwards-directed component, mass flow can be assumed to be more or less subhorizontal at depth, in contrast to the mass flow in the subduction channel, which follows the dip of the subduction zone. The occurrence of an exhumation channel in the Corsica–Sardinia Variscan belt has been hypothesized since by Massonne et al. [2018] and Scodina et al. [2019].

The geodynamic scenario proposed in this paper (Figure 11) follows that conceived by Massonne et al. [2018] and revised by Scodina et al. [2019] and Cruciani et al. [2021]. It intends to explain the different *P*–*T* path and peak pressure reached by the eclogites belonging to the medium-grade metamorphic complex and those of the Migmatite complex.

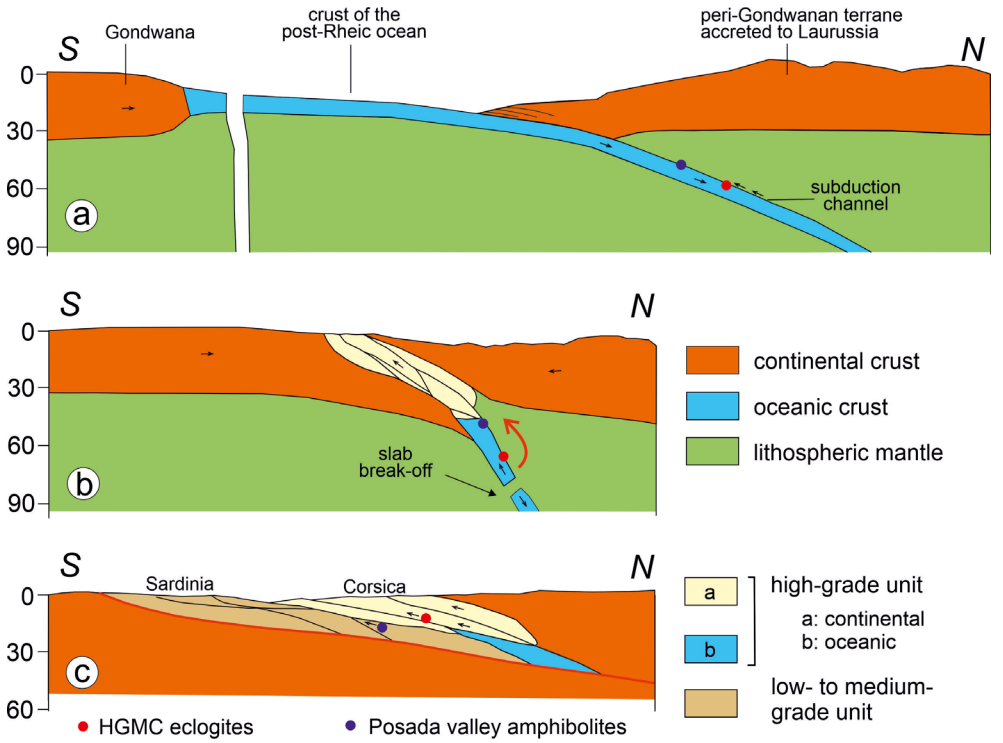

Figure 11. Geodynamic scenario reconstructed for the retrogressed eclogites and amphibolites from NE Sardinia [modified after Cruciani et al., 2021]. (a) Subduction of oceanic crust under a peri-Gondwanan terrane, previously accreted to Laurussia; Silurian–Devonian; (b) slab break-off and mantle upwelling (red arrow) after continental collision; late Devonian–early Carboniferous; (c) crustal thickening at the end of collision and exhumation of the Posada Valley amphibolites in the MGMC of the Corsica–Sardinia metamorphic belt; early–middle Carboniferous.

The geochemical signature of the different eclogitic lenses cropping out in Sardinia points to MORB and N-MORB protoliths [Cappelli et al., 1992, Cortesogno et al., 2004, Cruciani et al., 2015a] consistent with derivation from oceanic crust.

The protolith age of the Sardinian eclogites seems to be middle–upper Ordovician, as suggested by U–Pb zircon ages of Punta de Li Tulchi (457 ± 2 and 453 ± 14 Ma), Golfo Aranci (460 ± 5 Ma), and Giuncana (454 ± 6 Ma) eclogites, obtained by Cortesogno et al. [2004], Palmeri et al. [2004], Giacomini et al. [2005a] and Cruciani et al. [2015a], respectively. Palmeri et al. [2004], on the basis of SHRIMP zircon U–Pb data on the Punta de Li Tulchi eclogite (HGMC), hypothesized that the 400 ± 10 Ma might be the age of the eclogite formation in NE Sardinia. Giacomini et al. [2005b] interpreted early Visean zircon ages of retrogressed eclogites embedded in HGMC as related to HP, eclogite facies, metamorphic overprint.

The model that we propose starts with the subduction of oceanic crust under the peri-Gondwanan terrane which was previously accreted to Laurussia, in the Silurian–Devonian (Figure 11). The Posada Valley amphibolites were part of the oceanic crust of the subducting slab and reached maximum depths of 50 km (corresponding to the maximum of 1.4 GPa documented by *P*–*T* pseudosection modelling), while the eclogites of the HGMC reached greater depths of 65–70 km (Figure 11(a)). Convergence and subduction of oceanic crust in Silurian–Devonian times testified by eclogitic relics were also reported from the neighbouring terrains of the external crystalline Massifs (Western Alps) and from the Maures–Tanneron Massif in southern France [Guillot and Ménot, 2009 and references therein]. At this point,

the Posada Valley amphibolites likely, early reached the subduction channel or somehow were detached from the slab, probably by tectonic or subduction erosion before the eclogite facies conditions were reached and prior to the beginning of the collisional phase. After the continental collision, the slab break-off event occurred (Figure 11(b)), together with mantle upwelling (red arrow in Figure 11(b)) which caused heating of the HP slices of northern Sardinia and southern Corsica that were transported below the upper plate [Cruciani et al., 2021].

Subsequently, different slices of oceanic crust and continental crust from both upper and lower plates were brought together and tectonically mixed in an exhumation channel where they continued the uplift during the early and middle Carboniferous. The Posada Valley amphibolites emerged between the metamorphic complexes of NE Sardinia, while the eclogites further north were embedded between the rock units of the Migmatite complex (Figure 11(c)).

9. Concluding remarks

The Posada Valley amphibolites from the medium-grade metamorphic complex of NE Sardinia experienced a complex metamorphic history which resulted in a clockwise P–T evolution. These rocks record a prograde segment followed by an almost isothermal decompression from the metamorphic peak of 0.9–1.4 GPa at T = 530–690 °C (stage I), recorded by garnet composition, its inclusions and the Cpx+Pl assemblage, to a retrograde re-equilibration at amphibole stage conditions (stage II; P = 0.5–0.8 GPa and T = 620–720 °C), and a final stage (stage III) at greenschist facies conditions. The reconstructed P–T trajectory and the petrological features of the Posada Valley amphibolites (i.e., the absence of omphacite and the occurrence of plagioclase in every stage of the metamorphic evolution) exclude the full attainment of eclogite facies. These rocks were part of the oceanic crust of the subducting slab involved in the Variscan continental collision and subsequently exhumed together with continental slices from both upper and lower plates in an exhumation channel.

Acknowledgements

Financial support was provided by Regione Autonoma della Sardegna, L.R. 7/2007, research programme “Il blocco Sardo–Corso: area chiave per la ricostruzione della geodinamica varisica” CUP J81G17000110002.

Supplementary data

Supporting information for this article is available on the journal’s website under https://doi.org/10.5802/crgeos.65 or from the author.

References

Benisek, A., Dachs, E., and Kroll, H. (2010). A ternary feldspar-mixing model based on calorimetric data: development and application. *Contrib. Mineral. Petrol.*, 160, 327–337.

Blundy, J. D. and Holland, T. J. B. (1990). Calcic amphibole equilibria and a new amphibole–plagioclase geothermometer. *Contrib. Mineral. Petrol.*, 104, 208–224.

Cappelli, B., Carmignani, L., Castorina, F., Di Pisa, A., Oggiano, G., and Petrini, R. (1992). A Variscan suture zone in Sardinia: geological, geochemical evidence, Paleozoic Orogenies in Europe (special issue). *Geodin. Acta*, 5(1–2), 101–118.

Carmignani, L., Carosi, R., Di Pisa, A., Gattiglio, M., Musumeci, G., Oggiano, G., and Pertusati, P. C. (1994). The Hercynian chain in Sardinia (Italy). *Geodin. Acta*, 7, 31–47.

Carmignani, L., Oggiano, G., Barca, S., Conti, P., Eltrudis, A., Funedda, A., Pasci, S., and Salvadori, I. (2001). *Geologia della Sardegna. Note illustrative della Carta Geologica della Sardegna in scala 1:200,000,* volume LX of *Mem. Descrittive Carta Geol. It.*

Carosi, R. and Elter, F. M. (1989). Le microstrutture deformative di alto grado delle anfiboliti di Torpé (Sardegna NE). *Atti Soc. Toscana Sci. Nat., Memorie, Serie A*, 96, 241–255.

Carosi, R., Frassi, C., Iacopini, D., and Montomoli, C. (2005). Post collisional transpressive tectonics in northern Sardinia (Italy). *J. Virtual Explor.*, 19, article no. 3.

Carosi, R., Frassi, C., and Montomoli, C. (2009). Deformation during exhumation of medium- and high-grade metamorphic rocks in the Variscan chain in northern Sardinia (Italy). *Geol. J.*, 44, 280–305.

Carosi, R. and Palmeri, R. (2002). Orogen–parallel tectonic transport in the Variscan belt of northeastern Sardinia (Italy): implications for the exhumation of medium-pressure metamorphic rocks. *Geol. Mag.*, 139, 497–511.

Carosi, R., Petroccia, A., Iaccarino, S., Simonetti, M., Langone, A., and Montomoli, C. (2020). Kinematics and timing constraints in a transpressive tectonic regime: the example of the Posada-Asinara shear Zone (NE Sardinia, Italy). *Geosciences*, 10, article no. 288.

Casini, L., Cuccuru, S., Puccini, A., Oggiano, G., and Rossi, P. (2015). Evolution of the Corsica–Sardinia Batholith and late-orogenic shearing of the Variscides. *Tectonophysics*, 646, 65–78.

Connolly, J. A. D. (1990). Multivariable phase diagrams: an algorithm based on generalized thermodynamics. *Am. J. Sci.*, 290, 666–718.

Connolly, J. A. D. (2009). The geodynamic equation of state: what and how. *Geochem. Geophys. Geosyst.*, 10, article no. Q10014.

Corsi, B. and Elter, F. M. (2006). Eo–Variscan (Devonian?) melting in the high grade metamorphic complex of the NE Sardinia belt (Italy). *Geodin. Acta*, 3(4), 155–164.

Cortesogno, L., Gaggero, L., Oggiano, G., and Paquette, J. L. (2004). Different tectono-thermal evolutionary paths in eclogitic rocks from the axial zone of the Variscan chain in Sardinia (Italy) compared with the Ligurian Alps. *Ofioliti*, 29, 125–144.

Cruciani, G., Dini, A., Franceschelli, M., Puxeddu, M., and Utzeri, D. (2010). Metabasite from the Variscan belt in NE Sardinia, Italy: within-plate OIB-like melts with very high Sr and low Nd isotope ratios. *Eur. J. Mineral.*, 22, 509–523.

Cruciani, G., Fancello, D., Franceschelli, M., Scodina, M., and Spano, M. E. (2014). Geothermobarometry of Al–silicate bearing migmatites from the Variscan chain of NE Sardinia, Italy: a *P*–*T* pseudosection approach. *Period. Mineral.*, 83(1), 19–40.

Cruciani, G., Franceschelli, M., and Groppo, C. (2011). *P*–*T* evolution of eclogite-facies metabasite from NE Sardinia, Italy: insights into the prograde evolution of Variscan eclogites. *Lithos*, 121, 135–150.

Cruciani, G., Franceschelli, M., Groppo, C., Oggiano, G., and Spano, M. E. (2015c). Re-equilibration history and *P*–*T* path of eclogites from Variscan Sardinia, Italy: a case study from the medium-grade metamorphic complex. *Int. J. Earth Sci.*, 104, 797–814.

Cruciani, G., Franceschelli, M., Groppo, C., and Spano, M. E. (2012). Metamorphic evolution of non-equilibrated granulitized eclogite from Punta de li Tulchi (Variscan Sardinia) determined through texturally controlled thermodynamic modeling. *J. Metamorph. Geol.*, 30, 667–685.

Cruciani, G., Franceschelli, M., Langone, A., Puxeddu, M., and Scodina, M. (2015a). Nature and age of pre-Variscan eclogite protoliths from the low- to medium-grade metamorphic complex of north-central Sardinia (Italy) and comparison with coeval Sardinian eclogites in the northern Gondwana context. *J. Geol. Soc.*, 172, 792–807.

Cruciani, G., Franceschelli, M., Massonne, H.-J., Carosi, R., and Montomoli, C. (2013b). Pressure–temperature and deformational evolution of high-pressure metapelites from Variscan NE Sardinia, Italy. *Lithos*, 175–176, 272–284.

Cruciani, G., Franceschelli, M., Massonne, H.-J., and Musumeci, G. (2021). Evidence of two metamorphic cycles preserved in garnet from felsic granulite in the southern Variscan belt of Corsica, France. *Lithos*, 380–381, article no. 105919.

Cruciani, G., Franceschelli, M., Massonne, H.-J., Musumeci, G., and Scodina, M. (2020). Garnet-rich veins in an ultrabasic amphibolite from NE Sardinia, Italy: an example of vein mineralogical re-equilibration during the exhumation of a granulite terrane. *Geosciences*, 10, article no. 344.

Cruciani, G., Franceschelli, M., Massonne, H.-J., Musumeci, G., and Spano, M. E. (2016). Thermomechanical evolution of the high-grade core in the Nappe zone of Variscan Sardinia, Italy: the role of shear deformation and granite emplacement. *J. Metamorph. Geol.*, 34(4), 321–342.

Cruciani, G., Franceschelli, M., Musumeci, G., Spano, M. E., and Tiepolo, M. (2013a). U–Pb zircon dating and nature of metavolcanics and metarkoses from the Monte Grighini unit: new insights on Late Ordovician magmatism in the Variscan belt in Sardinia, Italy. *Int. J. Earth Sci.*, 102, 2077–2096.

Cruciani, G., Franceschelli, M., Scodina, M., and Puxeddu, M. (2019). Garnet zoning in kyanite-bearing eclogite from Golfo Aranci: new data on the early prograde *P*–*T* evolution in NE Sardinia, Italy. *Geol. J.*, 54, 190–205.

Cruciani, G., Montomoli, C., Carosi, R., Franceschelli,

M., and Puxeddu, M. (2015b). Continental collision from two perspectives: a review of Variscan metamorphism and deformation in northern Sardinia. *Period. Mineral.*, 84, 657–699.

Dale, J., Powell, R., White, R. W., Elmer, F. L., and Holland, J. B. (2005). A thermodynamic model for Ca–Na clinoamphiboles in Na_2O–CaO–FeO–MgO–Al_2O_3–SiO_2–H_2O–O for petrological calculations. *J. Metamorph. Geol.*, 23, 771–791.

Di Vincenzo, G., Carosi, R., and Palmeri, R. (2004). The relationship between tectono-metamorphic evolution and argon isotope records in white mica: constraints from *in situ* ^{40}Ar–^{39}Ar laser analysis of the Variscan basement of Sardinia. *J. Petrol.*, 45, 1013–1043.

Edel, J. B., Schulmann, K., Lexa, O., and Lardeaux, J. M. (2018). Late Palaeozoic palaeomagnetic and tectonic constraints for amalgamation of Pangea supercontinent in the European Variscan belt. *Earth-Sci. Rev.*, 177, 589–612.

Elter, F. M., Musumeci, G., and Pertusati, P. C. (1990). Late Hercynian shear zones in Sardinia. *Tectonophysics*, 176, 387–404.

Elter, F. M., Padovano, M., and Kraus, R. K. (2010). The Variscan HT metamorphic rocks emplacement linked to the interaction between Gondwana and Laurussia plates: structural constraints in NE Sardinia (Italy). *Terra Nova*, 22, 369–377.

Fancello, D., Cruciani, G., Franceschelli, M., and Massonne, H.-J. (2018). Trondhjemitic leucosomes in paragneisses from NE Sardinia: Geochemistry and *P*–*T* conditions of melting and crystallization. *Lithos*, 304–307, 501–517.

Faure, M., Rossi, P., Gaché, J., Melleton, J., Frei, D., Li, X., and Lin, W. (2014). Variscan orogeny in Corsica: new structural and geochronological insights, and its place in the Variscan geodynamic framework. *Int. J. Earth Sci.*, 103, 1533–1551.

Franceschelli, M., Memmi, I., Pannuti, F., and Ricci, C. A. (1989). Diachronous metamorphic equilibria in the Hercynian basement of northern Sardinia, Italy. In Daly, J. S., Cliff, R. A., and Yardley, B. W. D., editors, *Evolution of Metamorphic Belts*, volume 43 of *Geol. Soc. London, Special Publ.*, pages 371–375. Geological Society of London, London.

Franceschelli, M., Memmi, I., and Ricci, C. A. (1982). Ca distribution between garnet and plagioclase in pelitic and psammitic schists from the metamorphic basement of North-Eastern Sardinia. *Contrib. Mineral. Petrol.*, 80, 285–295.

Franceschelli, M., Puxeddu, M., and Cruciani, G. (2005). Variscan metamorphism in Sardinia, Italy: review and discussion. *J. Virtual Explor.*, 19, article no. 2.

Franceschelli, M., Puxeddu, M., Cruciani, G., and Utzeri, D. (2007). Metabasites with eclogite facies relics from Variscides in Sardinia, Italy: a review. *Int. J. Earth Sci.*, 96, 795–815.

Gerbault, M., Schneider, J., Reverso-Peila, A., and Corsini, M. (2018). Crustal exhumation during ongoing compression in the Variscan Maures-Tanneron Massif, France-Geological and thermo-mechanical aspects. *Tectonophysics*, 746, 439–458.

Giacomini, F., Bomparola, R. M., and Ghezzo, C. (2005a). Petrology and geochronology of metabasites with eclogite facies relics from NE Sardinia: constraints for the Palaeozoic evolution of Southern Europe. *Lithos*, 82, 221–248.

Giacomini, F., Bomparola, R. M., and Ghezzo, C. (2005b). The pre-Variscan magmatic-sedimentary history in the high-grade metamorphic basement of northern Sardinia (Italy): constraints from U/Pb geochronology and geochemistry. Epitome. In *Geoitalia 2005, Quinto Forum Italiano di Scienze della Terra. Spoleto, 21–23 September 2005*.

Green, E. C. R., Holland, T. J. B., and Powell, R. (2007). An order–disorder model for omphacitic pyroxenes in the system jadeite–diopside–hedenbergite–acmite with applications to eclogitic rocks. *Am. Mineral.*, 92, 1181–1189.

Guillot, S. and Ménot, R. P. (2009). Paleozoic evolution of the external crystalline Massifs of the Western Alps. *C. R. Geosci.*, 341, 253–265.

Hawthorne, F. C., Oberti, R., Harlow, G. E., Maresch, W. V., Martin, R. F., Schumacher, J. C., and Welch, M. D. (2012). IMA Report—Nomenclature of the amphibole supergroup. *Am. Mineral.*, 97, 2031–2048.

Holland, T. and Blundy, J. (1994). Non-ideal interactions in calcic amphiboles and their bearing on amphibole–plagioclase thermometry. *Contrib. Mineral. Petrol.*, 116, 433–447.

Holland, T. J. B., Baker, J. M., and Powell, R. (1998). Mixing properties and activity–composition relationships of chlorites in the system MgO–FeO–Al_2O_3–SiO_2–H_2O. *Eur. J. Mineral.*, 10, 395–406.

Holland, T. J. B. and Powell, R. (1996). Thermodynam-

ics of order–disorder in minerals, 2. Symmetric formalism applied to solid solutions. *Am. Mineral.*, 81, 1425–1437.

Holland, T. J. B. and Powell, R. (1998). An internally consistent thermodynamic data set for phases of petrological interest. *J. Metamorph. Geol.*, 16, 309–343.

Holland, T. J. B. and Powell, R. (2011). An improved and extended internally consistent thermodynamic dataset for phases of petrological interest, involving a new equation of state for solids. *J. Metamorph. Geol.*, 29, 333–383.

Liou, J. G., Zhang, R. Y., Ernst, W. G., Rumble Douglas, I. I. I., and Maruyama, S. (1998). High-pressure minerals from deeply subducted metamorphic rocks. In Hemley, R. J., editor, *Ultrahigh-Pressure Mineralogy*, volume 37 of *Rev. in Mineralogy*, pages 33–96. Mineralogical Society of America.

Massonne, H.-J. (2012). Formation of amphibole and clinozoisite–epidote in eclogite owing to fluid infiltration during exhumation in a subduction channel. *J. Petrol.*, 53(10), 1969–1998.

Massonne, H.-J. (2016). Hydration of the lithospheric mantle by the descending plate in a continent–continent collisional setting and its geodynamic consequences. *J. Geodyn.*, 96, 50–61.

Massonne, H.-J., Cruciani, G., and Franceschelli, M. (2013). Geothermobarometry on anatectic melts—a high-pressure Variscan migmatite from Northeast Sardinia. *Int. Geol. Review*, 55, 1490–1505.

Massonne, H.-J., Cruciani, G., Franceschelli, M., and Musumeci, G. (2018). Anticlockwise pressure–temperature paths record Variscan upper-plate exhumation: example from micaschists of the Porto Vecchio region. Corsica. *J. Metamorph. Geol.*, 36, 55–77.

Palmeri, R., Fanning, M., Franceschelli, M., Memmi, I., and Ricci, C. A. (2004). SHRIMP dating of zircons in eclogite from the Variscan basement in north-eastern Sardinia (Italy). *Neues Jahrb. Mineral. Monat.*, 6, 275–288.

Powell, R. and Holland, T. (1999). Relating formulations of the thermodynamics of mineral solid solutions: activity modeling of pyroxenes, amphiboles, and micas. *Am. Mineral.*, 84, 1–14.

Rossi, P., Oggiano, G., and Cocherie, A. (2009). A restored section of the "southern Variscan realm" across the Corsica–Sardinia microcontinent. *C. R. Geosci.*, 341, 224–238.

Schneider, J., Corsini, M., Reverso, P. A., and Lardeaux, J.-M. (2014). Thermal and mechanical evolution of an orogenic wedge during Variscan collision: an example in the Maures–Tanneron Massif (SE France). In Schulmann, K., Martinez Catalan, J. R., Lardeaux, J. M., Janousek, V., and Oggiano, G., editors, *The Variscan Orogeny: Extent, Timescale and the Formation of the European Crust*, volume 405 of *Geol. Soc. Lond., Special Publ.*, pages 313–331. The Geological Society of London, London.

Scodina, M., Cruciani, G., Franceschelli, M., and Massonne, H.-J. (2019). Anticlockwise *P*–*T* evolution of amphibolites from NE Sardinia, Italy: geodynamic implications for the tectonic evolution of the Variscan Corsica–Sardinia block. *Lithos*, 324–325, 763–775.

Scodina, M., Cruciani, G., Franceschelli, M., and Massonne, H.-J. (2020). Multilayer corona textures in the high-pressure ultrabasic amphibolite of Mt. Nieddu, NE Sardinia (Italy): equilibrium versus disequilibrium. *Period. Mineral.*, 89, 169–186.

Simonetti, M., Carosi, R., Montomoli, C., Corsini, M., Petroccia, A., Cottle, J. M., and Iaccarino, S. (2020). Timing and kinematics of flow in a transpressive dextral shear zone, Maures Massif (southern France). *Int. J. Earth Sci.*, 109, 2261–2285.

White, R. W., Powell, R., Holland, T. J. B., Johnson, T. E., and Green, E. C. R. (2014). New mineral activity–composition relations for thermodynamic calculations in metapelitic systems. *J. Metamorph. Geol.*, 32, 261–286.

White, R. W., Powell, R., Holland, T. J. B., and Worley, B. A. (2000). The effect of TiO_2 and Fe_2O_3 on metapelitic assemblages at greenschist and amphibolite facies conditions: mineral equilibria calculations in the system K_2O–FeO–MgO–Al_2O_3–SiO_2–H_2O–TiO_2–Fe_2O_3. *J. Metamorph. Geol.*, 18, 497–511.